Energy Storage Materials 74 (2025) 103930

Contents lists available at ScienceDirect

Energy Storage Materials

journal homepage: www.elsevier.com/locate/ensm

Enhancing structural flexibility in P2-type Ni-Mn-based Na-layered cathodes for high power-capability and fast charging/discharging performance

Bonyoung Ku [a,b,1], Jinho Ahn [a,b,1], Hoseok Lee [a,b], Hobin Ahn [a,b], Jihoe Lee [a,b], Hyunji Kweon [a,b], Myungeun Choi [a,b], Hun-Gi Jung [a,c,d], Kyuwook Ihm [e], Eunji Sim [a,e], Jung-Keun Yoo [c,*], Jongsoon Kim [a,b,c,d,*]

[a] Department of Energy Science, Sungkyunkwan University, Suwon 16419, Republic of Korea
[b] SKKU Institute of Energy Science and Technology, Sungkyunkwan University, Suwon 16419, Republic of Korea
[c] Energy Storage Research Center, Korea Institute of Science and Technology, Seoul 02792 Republic of Korea
[d] KIST-SKKU Carbon-Neutral Research Center, Sungkyunkwan University, Suwon, 16419, Republic of Korea
[e] Beamline Research Division, Pohang Accelerator Laboratory, POSTECH, Pohang 37673, Republic of Korea

ARTICLE INFO

Keywords:
Na-ion batteries
Oxygen redox
Stabilization
High voltage
First-principle calculation

ABSTRACT

P2-type Ni-Mn-based Na-layered cathodes suffer from severely large structural changes, such as the direct P2-O2 phase transition, occurring during charging to the high voltage region, resulting in the poor power-capability with large overpotential, as well as the diminished cycle-performance. In this study, through a combination of first-principles calculations and various experiments, we demonstrate that enhanced structural flexibility through Co-Al co-substitution provides smooth and continuous structural changes in the P2-type Ni-Mn-based Na-layered cathode without the direct phase transition, enabling the highly improved electrochemical performances. P2-type $Na_{0.67}[Ni_{0.35}Co_{0.1}Mn_{0.5}Al_{0.05}]O_2$ delivers a high discharge capacity of approximately ~156.31 mAh g^{-1} and an energy density of ~551.71 Wh kg^{-1} at 10 mA g^{-1}, outperforming P2-type $Na_{0.67}[Ni_{0.35}Mn_{0.65}]O_2$. These performance differences are especially pronounced during fast charging/discharging process, highlighting the enhanced power-capability and Na^+ diffusion kinetics due to improved structural flexibility. Moreover, smooth and continuous structural changes enable improved cycle performance, including reduced voltage decay during prolonged cycling, for P2-type $Na_{0.67}[Ni_{0.35}Co_{0.1}Mn_{0.5}Al_{0.05}]O_2$. These results highlight that introducing structural flexibility is one of the most efficient ways to enhance power-capability and fast-charging/discharging performance in P2-type Ni-Mn-based Na-layered cathodes, while also improving cyclability.

1. Introduction

The importance of environmentally friendly energy development is on the rise, along with active research in the field of energy storage systems [1–3]. Among these, lithium-ion batteries (LIBs) have gained prominence as the most promising energy storage solution due to their high energy density [4,5]. However, the sharp increase in lithium raw material prices and supply shortages has led to price hikes and a shortage of LIBs [6–8]. As a result, the development of new, cost-effective energy storage solutions has become imperative [9].

Among them, Na-ion batteries (SIBs) are emerging as a next-generation energy storage solution that can replace LIBs due to their cost-effectiveness, attributed to the abundant Na resources in the earth, and the monovalent-ion-based reaction mechanism similar to that of LIBs [10–13]. Recently, various cathode materials for SIBs have been reported, such as layered oxides, polyanion compounds, [14] Prussian blue analogue, [15] *etc*. Especially, in P2-type Ni-Mn-based Na-layered oxide cathodes with Ni contents of 0.3 mol or higher, it is possible to achieve high operating voltage and high energy density through the redox reaction between Ni^{2+} and Ni^{4+} during charge/discharge [16,17]. However, when only Ni and Mn are present in the layered structure, the interlayer distance in the Na layer is narrow, and due to the ratio of Ni to

* Corresponding authors.
E-mail addresses: yoojk@kist.re.kr (J.-K. Yoo), jongsoonkim@skku.edu (J. Kim).
[1] These authors contribute equally to this work.

https://doi.org/10.1016/j.ensm.2024.103930
Received 2 October 2024; Received in revised form 12 November 2024; Accepted 23 November 2024
Available online 24 November 2024

Mn [18], an ordered arrangement of Na^+/vacancy can occur, thus requiring significant energy for Na^+ de/intercalation at the structure [19]. Due to these characteristics, one of the Ni-Mn-based Na-layered cathode materials, P2-type $Na_{0.67}[Ni_{0.35}Mn_{0.65}]O_2$ (P2-NM), undergoes severe structural changes through a direct P2-O2 phase transition without formation of any intermediate phases during charge/discharge, which leads to poor cyclability and reduced power-capability, along with irreversible capacity loss [20]. Furthermore, the severe structural change induced by the direct P2-O2 phase transition results in large overpotential during charge/discharge, which leads to highly lowered available energy density during fast-discharging process [21,22].

Certainly, while simple metal-doping or -substitution has been shown to improve the cyclability of Ni-Mn-based Na-layered cathode materials like P2-NM by preventing the direct P2-O2 phase transition, it has generally been observed that suppressing the P2-O2 phase transition reduces the amount of reversibly usable Na contents in the structure, leading to decreased energy density and failing to improve power-capability [23,24]. Therefore, in this study, we focused on developing a strategy that enhances not only cyclability but also energy density and power-capability by introducing the structural flexibility with the enhanced ionic/electronic conductivity. It has been reported that the density of states (DOS) of O 2*p* and Co 3*d* orbitals can overlap in the layered oxide materials, enabling the excellent power-capability in $LiCoO_2$ [25]. Moreover, substitution of Co ions in the P2-NM structure can induce disorder in the ordered arrangement of Na^+/vacancy, mitigating the direct P2-O2 phase transition and resulting in a voltage plateau above 4.0 V (*vs.* Na^+/Na) during charge/discharge [26–28]. Additionally, upon substitution into the structure, kinetic enhancement can lead to improvements in high-rate performance [29]. Furthermore, Al ions with fixed oxidation state of +3 do not experience changes in the bonding interaction with oxygen anions during charge/discharge, thereby enhancing the structural stability [30,31]. Additionally, these ions can cause disorder in the ordered arrangement of Na^+/vacancy, further improving the structural stability and cyclability of the layered oxide cathodes [32].

Thus, it was expected that the synergy of Co-Al co-substitution in P2-NM could successfully provide both high structural stability by preventing the direct P2-O2 phase transition and enabling continuous structural change with the formation of intermediate phases during charge/discharge, as well as enhanced Na^+ diffusion kinetics for high power-capability. To demonstrate our strategy, we prepared P2-type $Na_{0.67}[Ni_{0.35}Co_{0.1}Mn_{0.5}Al_{0.05}]O_2$ (P2-NCMA) and investigated its enhanced electrochemical performances. At a current density of 10 mA g^{-1} in a voltage range of 2.2–4.35 V (*vs.* Na^+/Na), P2-NCMA exhibited the large discharge capacity and discharge energy density of ~156.31 mAh g^{-1} and ~551.71 Wh kg^{-1}, respectively, which are larger than those of P2-NM (~145.60 mAh g^{-1} and ~526.98 Wh kg^{-1}) under the same conditions. Even at 1000 mA g^{-1}, the discharge capacity of P2-NCMA was ~132.38 mAh g^{-1}, whereas P2-NM just deliver the capacity of ~94.31 mAh g^{-1}. More interesting point is that difference of the energy density between P2-NCMA and P2-NM at 1000 mA g^{-1} was ~154.60 Wh kg^{-1}, which is due to the difference in the electrochemical behavior at high voltage (>4.1 V *vs.* Na^+/Na) operation. P2-NCMA also delivered highly improved cycle-performance compared to P2-NM. Through first-principles calculation and *operando* XRD analyses, it was revealed that P2-NCMA experiences the continuous and smooth structural change with formation of intermediate phases during charging/discharging, even in the high voltage region above 4.1 V, whereas clear two-phase reaction between P2 and O2 phases occurred in P2-NM under same conditions. These results indicate the enhanced power-capability and fast charging/discharging performance of P2-NCMA through introduction of structural flexibility. These findings were further supported by a comparison of theoretical density of states (DOSs) and Na^+ diffusion barrier energies between fully Na^+-deintercalated P2-NCMA and P2-NM. Additionally, through synchrotron-based X-ray absorption near edge structure (XANES) and the extended X-ray absorption fine structure (EXAFS) analyses, the reversible redox mechanism and stabilization of local environment during charge/discharge processes were demonstrated, which provides the insights for understanding the improved electrochemical performances.

2. Material and methods

2.1. Synthesis of P2-$Na_{0.67}[Ni_{0.35}Co_{0.1}Mn_{0.5}Al_{0.05}]O_2$, P2-$Na_{0.67}[Ni_{0.35}Co_{0.1}Mn_{0.55}]O_2$ and P2-$Na_{0.67}[Ni_{0.35}Mn_{0.65}]O_2$

P2-$Na_{0.67}[Ni_{0.35}Co_xMn_{0.65-x-y}Al_y]O_2$ [(*x, y*) = (0, 0), (0.1, 0), (0, 0.05) and (0.1, 0.05)] compounds was prepared using the solid-state method. Na_2CO_3 (Sigma Aldrich, 99.5 %), $Ni(OH)_2$ (Samchun Chemical, 98 %), CoC_2O_4 (Alfa Aesar, 98 %), $MnCO_3$ (Alfa Aesar, 99 %) and Al_2O_3 (Alfa Aesar, 99 %) were used as precursors. 5 mol% of Na_2CO_3 was additionally added to compensate for the loss of sodium during calcination. The precursors were carefully blended in stoichiometirc ratio using a high-energy ball milling apparatus, operating at 400 rpm for 12 h with silicon-nitride balls. Following the thorough mixing process, the resulting uniformly mixed powder was shaped into pellets using a pressure machine, then subjected to calcination in an O_2 gas atmosphere at a temperature of 850 °C for 12 h (heating rate of 2.5 °C min^{-1}).

2.2. Materials characterization

The crystal structure of P2-$Na_{0.67}[Ni_{0.35}Co_xMn_{0.65-x-y}Al_y]O_2$ [(*x, y*) = (0, 0), (0.1, 0) and (0.1, 0.05)] were examined through X-ray diffraction (XRD) using a PANalytical instrument with Mo Kα radiation (wavelength = 0.70932 Å). The data were collected in the 2θ range of 4.61° to 34.32° with a 0.013° step size. Subsequently, the XRD patterns were reevaluated by converting the angles to Cu Kα radiation (wavelength = 1.54178 Å) for comparison with prior research. The XRD refinement data were analyzed using the Foolproof Rietveld program. *Operando* XRD patterns were acquired to monitor structural changes during charge/discharge at a current density of 20 mA g^{-1} within the voltage range of 2.2–4.35 V (*vs.* Na^+/Na). These *operando* XRD patterns were collected using an X-ray diffractometer (PANalytical Empyrean) equipped with Mo Kα radiation (wavelength = 0.70932 Å). The data were collected in the 2θ range of 4.0° to 35.0° with a step size of 0.013° and reevaluated by converting the angles to Cu Kα radiation (wavelength = 1.54178 Å). The elemental composition of substances like Na, Ni, Co, Mn and Al was analyzed using an inductively coupled plasma atomic emission spectrometer (ICP-AES; OPTIMA 8300, Perkin-Elmer). The morphology of the materials was examined using a Field emission scanning electron microscopy (FE-SEM) (Gemini SEM 560, ZEISS) at 2 keV, conducted at the National Center for Inter-University Research Facilities (NCIRF) affiliated with Seoul National University. Additionally. High resolution transmission electron microscopy (HR-TEM) image, energy-dispersive X-ray spectroscopy (EDS) mappings and selective area electron diffraction (SAED) Pattern were measured by 200 kV STEM (JEM-ARM300F, JEOL) at the Advanced Facility Center for Quantum Technology at the Sungkyunkwan University. Prior to the measurements, the samples were dispersed in ethanol with the aid of an ultrasonic device. Following this, a droplet of the suspension was applied onto a copper TEM grid coated with carbon, and the grid was left to air-dry at room temperature overnight to facilitate the evaporation of ethanol.

2.3. Electrochemical characterization

P2-$Na_{0.67}[Ni_{0.35}Co_xMn_{0.65-x-y}Al_y]O_2$ [(*x, y*) = (0, 0), (0.1, 0), (0, 0.05) and (0.1, 0.05)] electrodes were prepared by blending 80 wt% active material, 10 wt% Super P carbon black, and 10 wt% polyvinylidene fluoride (PVDF) with N-methyl-2-pyrrolidone (NMP) as the solvent. The resulting mixture was then coated onto aluminum foil and dried under vacuum conditions at 100 °C overnight. After drying, the

electrodes were cut into disks with a diameter of 10 π-mm, and each electrode had a mass loading of approximately 3 mg cm^{-2}. For the assembly of half-cells, CR2032-type coin cells were employed. These cells included Na metal as the counter electrode, a separator made of Whatman GF/F glass fiber, and an electrolyte comprising 1M $NaPF_6$ in a solvent mixture of propylene carbonate (PC) and fluoroethylene carbonate (FEC) in a ratio of 98:2 (v/v). The coin cells were assembled inside an argon-filled glove box. Galvanostatic charge/discharge tests were conducted at various current densities (ranging from 10 to 1000 mA g^{-1}) in the voltage window of 2.2–4.35 V (*vs.* Na^+/Na). To prevent the overpotential by transitioning from charge to discharge, the voltage was maintained until the charge current density dropped to the value corresponding to 10 mA g^{-1}. Battery cycling tests were carried out using an automated battery charge/discharge test system (WBCS 3000, WonATech). After the initial charge/discharge cycle, the cycling performance was assessed at a current density of 100 mA g^{-1}. P2-$Na_{0.67}[Ni_{0.35}Co_{0.1}Mn_{0.5}Al_{0.05}]O_2$ underwent *ex-situ* X-ray absorption spectroscopy (XAS) analysis at the Ni K-edge, Co K-edge, and Mn K-edge. These analyses were conducted at the 6D XAFS and 7D XAFS beamline located within the Pohang Accelerator Laboratory (PAL), utilizing Ni, Co, and Mn metal foils as reference spectra. The XAS spectra were collected in transmission mode under high electron energy conditions (2.5 GeV) with a current of 200 mA, covering both the X-ray absorption near-edge structure (XANES) and extended X-ray absorption fine structure (EXAFS) regions. Furthermore, Ni L-edge and Co L-edge total electron yield photoemission spectroscopy (TEY-PES) were measured by the 8A1-SPEM beam line at PAL. Additionally, soft X-ray absorption spectroscopy (sXAS) spectra for the O K-edge were measured at the 4D-

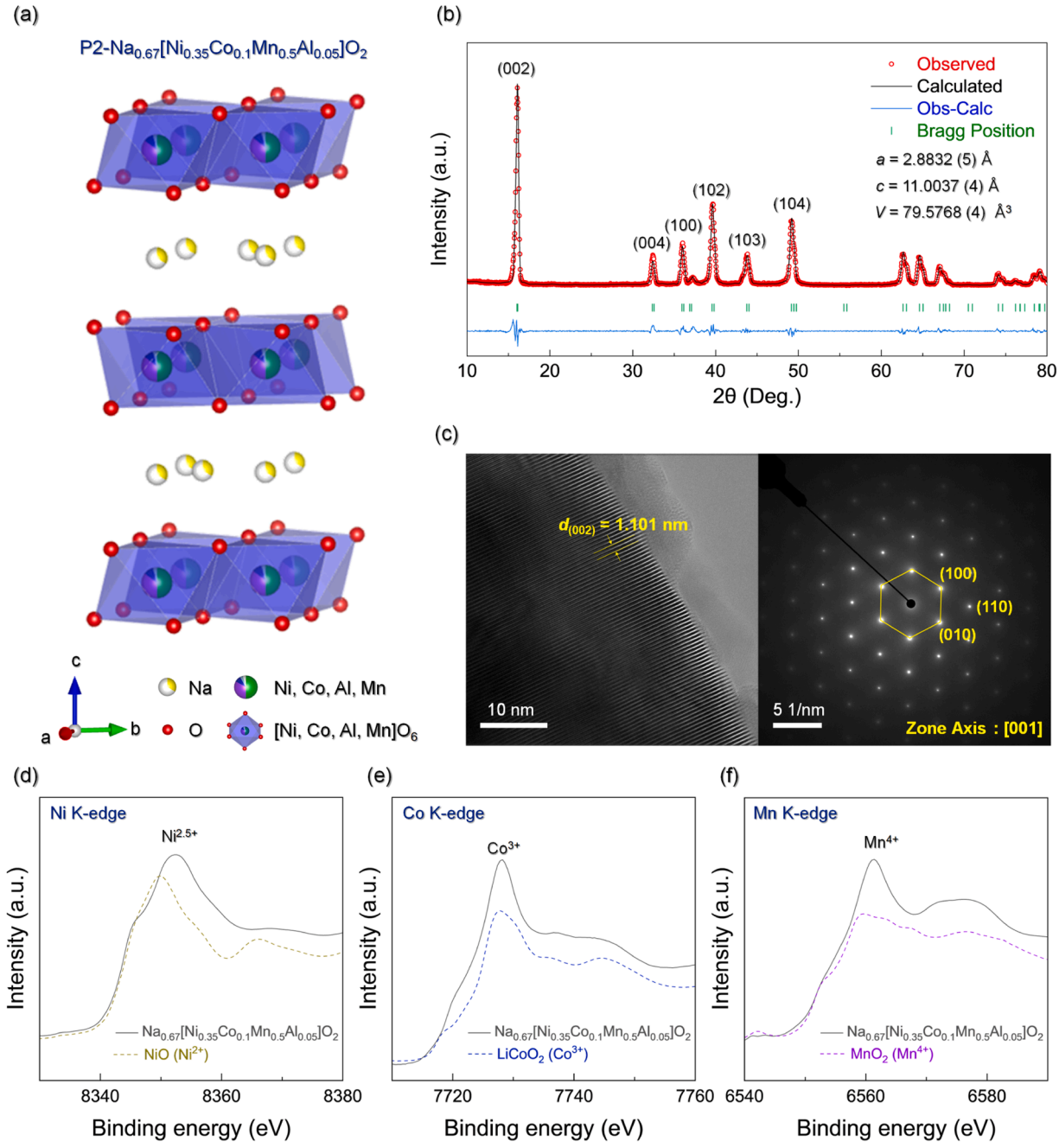

Fig. 1. (a) Crystal structure of P2-$Na_{0.67}[Ni_{0.35}Co_{0.1}Mn_{0.5}Al_{0.05}]O_2$. (b) XRD pattern and Rietveld refinement results of P2-$Na_{0.67}[Ni_{0.35}Co_{0.1}Mn_{0.5}Al_{0.05}]O_2$ (R_p = 2.63 %, R_{wp} = 2.40 %, χ^2 = 2.72). (c) HR-TEM image of P2-$Na_{0.67}[Ni_{0.35}Co_{0.1}Mn_{0.5}Al_{0.05}]O_2$ and SAED pattern. Pristine K-edge of (d) Ni, (e) Co, (f) Mn.

PES beamline at PAL with a photon energy range of 525–560 eV Subsequently, data obtained from both XAFS and SPEM analyses were subjected to analysis using the Athena software. It's worth noting that the samples were prepared in the form of an electrode.

2.4. Computational details

The Vienna Ab Initio Simulation Package (VASP) was employed for all density functional theory (DFT) calculations concerning P2-$Na_{0.67}[Ni_{0.35}Co_{0.1}Mn_{0.5}Al_{0.05}]O_2$ [33]. These calculations used projector-augmented wave (PAW) pseudopotentials along with a plane wave basis integrated into VASP [34]. The Perdew–Burke–Ernzerhof (PBE) parameterization of the generalized gradient approximation (GGA) was utilized to describe the exchange-correlation functional [35]. The structural calculations considered a 2×2×1 supercell of P2-$Na_{0.67}[Ni_{0.35}Co_{0.1}Mn_{0.5}Al_{0.05}]O_2$ and were conducted with a 5×4×3 K-point grid. To account for the localization of *d*-orbitals in Ni, Co, and Mn ions, the GGA+U method was implemented with effective U values of 4.0, 3.4, and 3.9, respectively [36]. The Heyd-Scuseria-Ernzerhof (HSE06) equation was utilized to precisely compute the projected density of states (pDOS) for Ni, Co, Mn and O ions [37]. Additionally, the configurations of Na^+/Va at each composition were generated using CASM software, and up to 20 configurations at each composition were subsequently subjected to density functional theory (DFT) calculations [38].

3. Result and discussion

3.1. Preparation of P2-$Na_{0.67}[Ni_{0.35}Co_{0.1}Mn_{0.5}Al_{0.05}]O_2$ (P2-NCMA)

P2-NCMA was synthesized using a conventional solid-state synthesis method. As shown in Fig. 1a, the crystal structure of P2-NCMA exhibits the typical P2-type layered structure with ABBA oxygen stacking sequence and a well-ordered hexagonal structure characterized by space group of $P6_3/mmc$. XRD analysis and Rietveld refinement further confirmed well-preparation of P2-NCMA with no impurities (Fig. 1b). The lattice parameters of $a(=b)$ and c were ~2.8832(5) Å and ~11.0037 (4) Å, respectively. Detailed structural information, such as thermal factors (B_{iso}), occupancy and atomic coordinate, were tabulated in Table S1. In P2-type layered cathodes, Na^+/vacancy ordering can occur when the ratio of Ni to Mn approaches 1:2, driven by the charge ordering of transition metals. At this point, the sites of Na_f, which are face-sharing with TMO_6, occupy 1/6 of the total Na sites, leading to the formation of new planes with d-spacing values of 3.13 Å and 3.25 Å As a result, peaks are known to appear at approximately 27.3° and 28.4° [18,19]. However, in the XRD pattern of P2-NCMA, no XRD peaks indicating Na^+/vacancy ordering were observed. This suggests that the substitution of Co and Al ions within the P2-NCMA structure altered the Ni:Mn ratio and modified the charge ordering of the transition metals, resulting in a disordered Na^+/vacancy arrangement. Furthermore, this implies that Co-Al co-substitution provides structural flexibility in Ni-Mn-based Na-layered cathode materials. The P2-type layered structure of P2-NCMA was also confirmed through HR-TEM and SAED analyses (Fig. 1c). Upon examination of SEM analysis (Fig. S1), it was observed that the particle size of P2-NCMA is approximately 0.5 μm. Additionally, TEM-based EDS elemental mapping analysis indicates that the Na, Ni, Co, Mn and Al elements are homogeneously distributed in the P2-NCMA particle with the elemental ratio of Na : Ni : Co: Mn: Al = 0.67: 0.35: 0.1: 0.5: 0.05 (Fig. S2). The elemental ratio in the P2-NCMA was also confirmed through ICP-AES analysis (Table S2). To investigate the oxidation states of the transition metal (TM) ions in the P2-NCMA, XANES experiments were conducted. As shown in Fig. 1d-f, it was verified that the Ni, Co and Mn ions in the P2-NCMA have the oxidation state of approximately 2.5+, 3+ and 4+, respectively. In addition, we prepared the P2-$Na_{0.67}[Ni_{0.35}Mn_{0.65}]O_2$ (P2-NM) as the control group using the same synthesis method with P2-NCMA. Fig. S3–4 and Table S3 show the refined XRD pattern and SEM image of P2-NM. It was confirmed that P2-NM was well-prepared with P2-type layered structure and the particle size of ~0.5 μm, consistent with P2-NCMA. Moreover, unlike P2-NCMA, some peaks are observed at ~27.3° and ~28.4° in the XRD pattern of P2-NM, which indicates introduction of the Na^+/vacancy ordering in P2-NM [19]. Additionally, when comparing the initial oxidation states of Ni ions in P2-NCMA and P2-NM, it was found that P2-NCMA showed a shift toward the higher energy region at the Ni K-edge due to Co and Al substitution, along with a distinct difference in the overall profile (Fig. S5) [39]. This indicates a clear difference in the initial Ni oxidation states of the two materials.

3.2. Enhanced electrochemical properties of P2-$Na_{0.67}[Ni_{0.35}Co_{0.1}Mn_{0.5}Al_{0.05}]O_2$

To confirm enhanced electrochemical performances through introduction of structural flexibility in Ni-Mn-based P2-type layered oxide cathodes, we compared the power-capability of P2-NCMA and P2-NM. Fig. S6 shows the initial charge/discharge curve of P2-NCMA, and P2-NM measured at the current density of 10 mA g^{-1} in the voltage range of 2.2–4.35 V (*vs.* Na^+/Na). It was observed that P2-NCMA exhibits the discharge capacity of ~156.31 mAh g^{-1} with the initial Coulombic efficiency of ~96 %, which is better than the discharge capacity and initial Coulombic efficiency of P2-NM (~145.60 mAh g^{-1} and ~89 %, respectively). Moreover, the charge/discharge profiles of P2-NCMA were significantly smooth compared to P2-NM, implying that the local environmental changes caused by Na^+/vacancy ordering during charge/discharge are mitigated in P2-NCMA compared to P2-NM [40].

As shown in Fig. 2a-b and Fig. S7–8, the difference of the capacity between P2-NCMA and P2-NM gets larger and larger with increasing the current densities, indicating more outstanding power-capability of P2-NCMA compared to P2-NM. Even under 1000 mA g^{-1}, P2-NCMA delivered the large discharge capacity of ~132.38 mAh g^{-1}, whereas the discharge capacity of P2-NM was just ~94.31 mAh g^{-1}. Particularly, the difference in the average discharge voltage measured in the high voltage region at 10 and 1000 mA g^{-1} was only ~0.23 V. On the other hand, in the case of P2-NM, the difference under the same conditions was ~0.78 V, which are larger than P2-NCMA. The enhanced power-capability of P2-NCMA was also demonstrated through comparing the energy densities measured at the various current densities (Fig. 2c). The energy densities were calculated through integration of the discharge curve based on voltage (V) *vs.* capacity (mAh g^{-1}). In the case of P2-NCMA, it exhibited the large energy density of ~555.11 Wh kg^{-1} at 10 mA g^{-1}, while NM just delivered ~527.00 Wh kg^{-1} under the same conditions. In particular, as the current density increased, the difference of energy densities between two samples became more pronounced. For P2-NCMA, even at 1000 mA g^{-1}, it displayed a substantial energy density of ~440.90 Wh kg^{-1}. On the other hand, P2-NM exhibited a low energy density of ~286.31 Wh kg^{-1} at the same current density. In addition, we tested the power-capability of P2-$Na_{0.67}[Ni_{0.35}Co_{0.1}Mn_{0.55}]O_2$ (P2-NCM) where only Co ion was substituted. The XRD and refined results in Fig. S9 and Table S4 show that P2-NCM are well prepared with pure P2-type layered structure. As shown in Fig. S10, it was verified that the P2-NCM exhibited poor power-capability and fast charging/discharging performances compared to P2-NCMA, while its performances are better than P2-NM. Furthermore, we measured the power-capability and cyclability of P2-$Na_{0.67}[Ni_{0.35}Mn_{0.6}Al_{0.05}]O2$ (P2-NMA), where only the Al ion was substituted. The XRD Rietveld refinement results presented in Fig. S11 and Table S5 show that P2-NMA was well synthesized with a pure P2-type layered structure. It was also confirmed that the peaks corresponding to Na^+/vacancy ordering at 27.3° and 28.4°, which were observed in P2-NM, disappeared through Al-substitution [32,41]. As shown in Fig. S12a-b, the results revealed that when Al ions were substituted, the difference in the average discharge voltage measured in the high voltage region at 10 and 1000 mA g^{-1} was reduced, but no improvement in capacity was observed. Additionally, a similar capacity

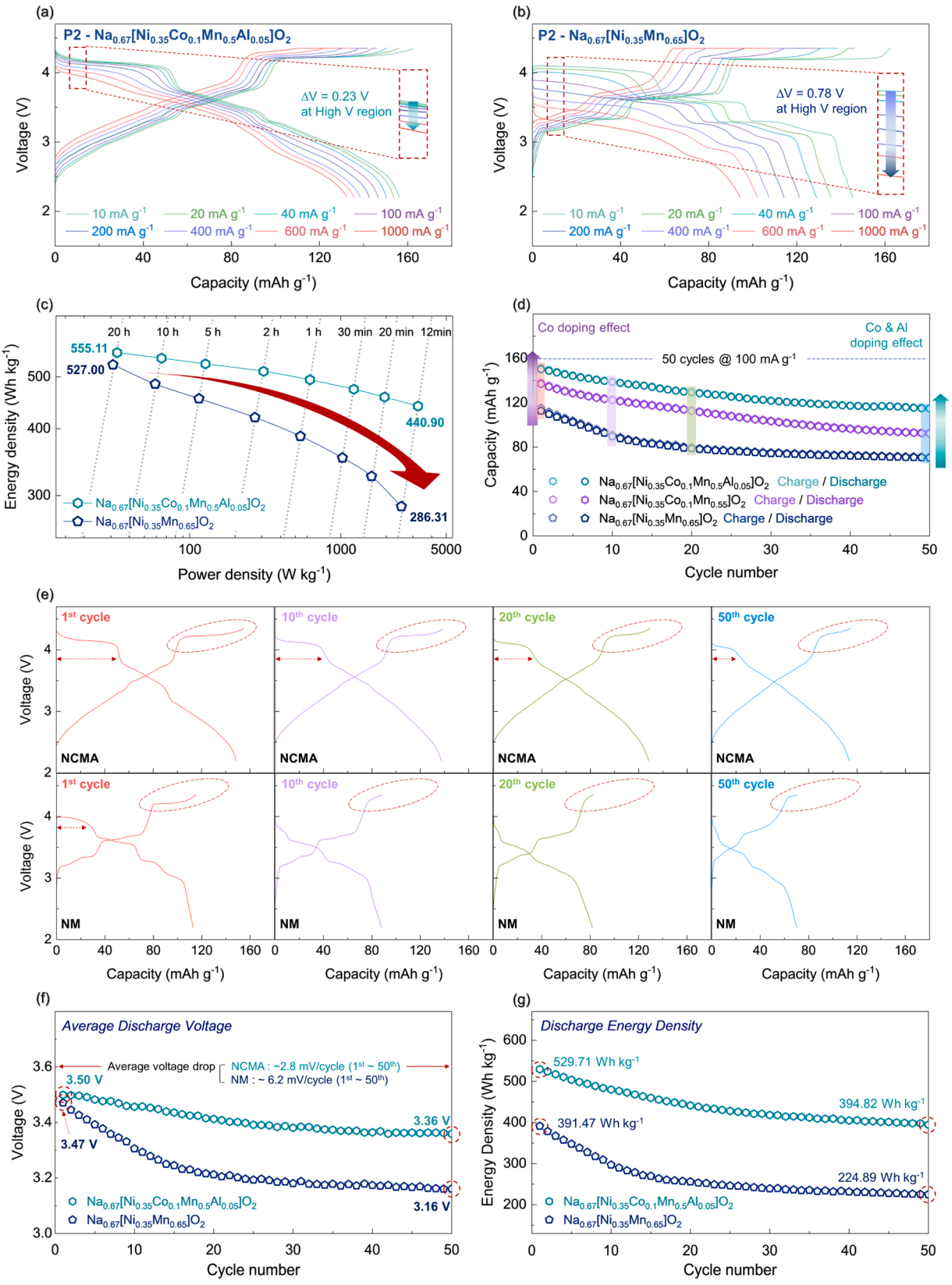

Fig. 2. Charge/Discharge profiles of (a) P2-$Na_{0.67}[Ni_{0.35}Co_{0.1}Mn_{0.5}Al_{0.05}]O_2$, (b) P2-$Na_{0.67}[Ni_{0.35}Mn_{0.65}]O_2$ in the voltage range of 2.2–4.35 V (*vs.* Na^+/Na) at various current densities, where the high V region refers to the voltage range up to the point at which a capacity of 20 mAh g^{-1} is achieved. (c) Energy density and power density of P2-$Na_{0.67}[Ni_{0.35}Co_{0.1}Mn_{0.5}Al_{0.05}]O_2$ and P2-$Na_{0.67}[Ni_{0.35}Mn_{0.65}]O_2$ at various current densities. (d) Cycle performances in the voltage range of 2.2–4.35 V (*vs.* Na^+/Na) during 50 cycles at 100 mA g^{-1} (e) 1st, 10th, 20th and 50th cycle profiles of P2-$Na_{0.67}[Ni_{0.35}Co_{0.1}Mn_{0.5}Al_{0.05}]O_2$ and P2-$Na_{0.67}[Ni_{0.35}Mn_{0.65}]O_2$. (f) Average discharge voltage and (g) discharge energy density of P2-$Na_{0.67}[Ni_{0.35}Co_{0.1}Mn_{0.5}Al_{0.05}]O_2$ and P2-$Na_{0.67}[Ni_{0.35}Mn_{0.65}]O_2$ during 50 cycles at 100 mA g^{-1}.

fade after the initial activation, as observed in P2-NM, was noted. Nevertheless, the suppression of Na^+/vacancy ordering improved structural stability, allowing for higher capacity retention during the cycle test compared to P2-NM. These results imply Co-Al co-substitution in the Ni-Mn-based P2-type layered oxide cathode can successfully suppresses Na^+/vacancy ordering, thereby enhancing the structural flexibility, enabling highly enhanced Na^+ diffusion kinetics and power-capability in P2-NCMA.

The synergy of Co-Al co-substitution can affect not only enhancing the power-capability but also stabilizing the cycle-performances. To compare the cycling performance of P2-NM, P2-NCM and P2-NCMA, we initially carried out a single activation process at a current density of 10 mA g^{-1}, followed by continuous charge/discharge cycling at a current density of 100 mA g^{-1} for 50 cycles in the voltage range of 2.2–4.35 V (*vs.* Na^+/Na) (Fig. 2d). P2-NM exhibited a low initial capacity when charge/discharge cycling was performed after the initial activation, which is attributed to the poor Na^+ diffusion kinetics in P2-NM containing the Na^+/vacancy ordering in the structure. On the other hand, P2-NCMA exhibited not only larger initial capacity than P2-NM and P2-NCM but also more stable cycle-performance. To gain a more in-depth understanding, a comparative assessment of the cycling profiles between P2-NCMA and P2-NM was carried out (Fig. 2e). After closely examining the charge and discharge profiles over 1st, 10th, 20th, and 50th cycles, it was observed that P2-NCMA exhibited relatively well-retained capacity in the high voltage region throughout the cycling. In contrast, as previously mentioned, P2-NM initially showed low capacity in this region. Especially, as the cycles progressed, it exhibited highly degraded capacity in the high voltage region. The difference in cycling profiles between P2-NCMA and P2-NM was even more pronounced in the differential capacity *versus* voltage (dQ/dV) graphs (Fig. S13). In the case of P2-NCMA, as cycling progresses from the first cycle to the 50th cycle, there is a tendency for voltage hysteresis to increase and the peak in the high voltage region to gradually decrease. However, for P2-NM, it was observed that peaks appear below 4.0 V from the beginning of the discharge process, and as cycling continues, a significant reduction in charge and discharge peaks in the high voltage region was observed. This result implies the occurrence of severe structural degradation in P2-NM after cycling. Additionally, comparing the average discharge voltage over 50 cycles measured at a current density of 100 mA g^{-1}, P2-NCMA showed an average discharge voltage decrease of ~2.8 mV per cycle, whereas P2-NM exhibited an average discharge voltage decrease of ~6.2 mV per cycle (Fig. 2f). This indicates much better voltage retention in P2-NCMA, with a significant average voltage difference of ~0.14 V after 50 cycles. Moreover, when calculating the average discharge energy density over 50 cycles, P2-NCMA still delivered a large energy density of ~394.82 Wh kg^{-1}, while P2-NM showed a low energy density of ~224.89 Wh kg^{-1} (Fig. 2g). These results indicate that P2-NCMA exhibits stable cycle-performance compared to P2-NM. Additionally, we conducted a cycle test at a high current density of 400 mA g^{-1} to confirm the enhanced fast charging/discharging performance of P2-NCMA. During the cycle test, P2-NCMA exhibited an impressive initial capacity exceeding 140 mAh g^{-1}, with a respectable capacity retention of ~71.07 % after 100 cycles. In contrast, P2-NM displayed a much lower initial capacity of 90 mAh g^{-1} and a significantly lower capacity retention of ~60.33 % after 100 cycles (Fig. S14). Additionally, when comparing the average discharge voltage, P2-NCMA showed a minimal voltage drop of ~2.4 mV per cycle, whereas P2-NM exhibited a more pronounced voltage drop of ~4.3 mV per cycle (Fig. S15). These findings demonstrate the outstanding fast charging/discharging performance of P2-NCMA even under high current density conditions.

3.3. Enhanced structural stability of P2-$Na_{0.67}[Ni_{0.35}Co_{0.1}Mn_{0.5}Al_{0.05}]O_2$ through increased flexibility

To confirm that the enhanced power-capability and fast charging/discharge performance in P2-NCMA, as well as improved cycle-performance result from introduction of structural flexibility, we investigated the detailed structural change in P2-NCMA through *operando* XRD analyses and compared it with that in P2-NM. As shown in Fig. 3a and 3c, both P2-NCMA and P2-NM experience similar structural change during charging to 4.0 V, such as increase of *c*-lattice parameter due to repulsion between O^{2-} anions. However, during charging/discharging at the high voltage region between 4.0 and 4.35 V, the structural changes of P2-NCMA and P2-NM have large difference. In the case of P2-NCMA, a new XRD peak at ~17° corresponding to OP4 phase was firstly formed during charging at the high voltage region, and it smoothly shifted to ~18.4° with formation of several intermediate phases (Fig. 3b). On the other hand, P2-NM experienced clear two-phase reaction from P2 phase to O2 phase without formation of any intermediate phases. Formation of O2 phase could be confirmed through generation of a new XRD peak at ~20° (Fig. 3d), which indicates more severe structural change of P2-NM during charge/discharge compared to P2-NCMA. Especially, in the case of P2-NM, there is no continuous structural change during charging/discharging at the high voltage region between 4.0 and 4.35 V, such as shift of the XRD peak on the O2 phase, which is clearly distinct from the structural change of P2-NCMA. These results indicate that the P2-NM with Na^+/vacancy ordering lacks the structural flexibility, hindering smooth expansion/shrinkage of the Na layers and adversely affecting the Na^+ de/intercalation process, and Co and Al co-substitution can provide the structural flexibility to enable enhanced electrochemical performances in P2-NCMA. Moreover, we calculated the lattice parameters and volumes on the *operando* XRD pattens of P2-NCMA and P2-NM using Rietveld refinement (Fig. S16 and S17), which clearly shows larger structural change of P2-NM during charge/discharge compared to P2-NCMA.

In addition, to evaluate the degree of structural changes occurring as cycling progresses, *ex-situ* experiments were conducted at 1st, 10th, 20th, and 50th cycles. For P2-NCMA, it was observed that as the cycles advanced, the material retained its original peak positions, and the intensity of the XRD peak corresponding to (002) plane remained consistently high (Fig. S18). However, in the case of P2-NM, as the cycles proceeded, there was a noticeable shift in the peak positions, and the intensity of the XRD peak corresponding to (002) plane gradually decreased (Fig. S19). Furthermore, upon examining SEM images of the pristine, 1st-cycled, and 50th-cycled samples, it was observed that in the case of P2-NCMA, the particles maintained their shape without surface cracks (Fig. S20). However, for P2-NM, even in the 1st-cycled sample, slight surface cracks were visible, and after 50 cycles, the severity of cracking became considerably pronounced (Fig. S21). This indicates that P2-NCMA, with its flexible structure, maintained stability without degradation and failure during prolonged cycling, whereas P2-NM, lacking structural flexibility, experienced rapid degradation and particle collapse.

To analyze this phenomenon from a more microscopic perspective, we examined the changes in TM-O bond distances in both the pristine state and the fully Na-deintercalated state through first-principles calculation (Fig. 3e-f). The crystal structures of the pristine state and the fully Na-deintercalated state in P2-NCMA and P2-NM, obtained through DFT calculations, are visualized in Fig. S22–23. In the case of P2-NCMA, we observed that the bond distances of TM-O bonds are evenly distributed in the pristine state due to the substitution of Co and Al ions. This suggests a high level of entropy within the TM layers, which contributes to improved structural stability [42]. Even in the fully Na-deintercalated state, although the degree of bond distance distribution slightly decreased due to the oxidation of transition metals, the bond distances remain relatively evenly distributed. In contrast, for P2-NM, we found that TM-O bond distances are clearly separated in the pristine state. Particularly in the case of Ni, a distortion in the NiO_6 octahedra was observed, indicating structural instability. Even in the fully Na-deintercalated state, the bond distances of Ni and Mn remained separated. This indicates that P2-NCMA, through the disordered distribution of TM-O bond distances, achieves enhanced structural flexibility,

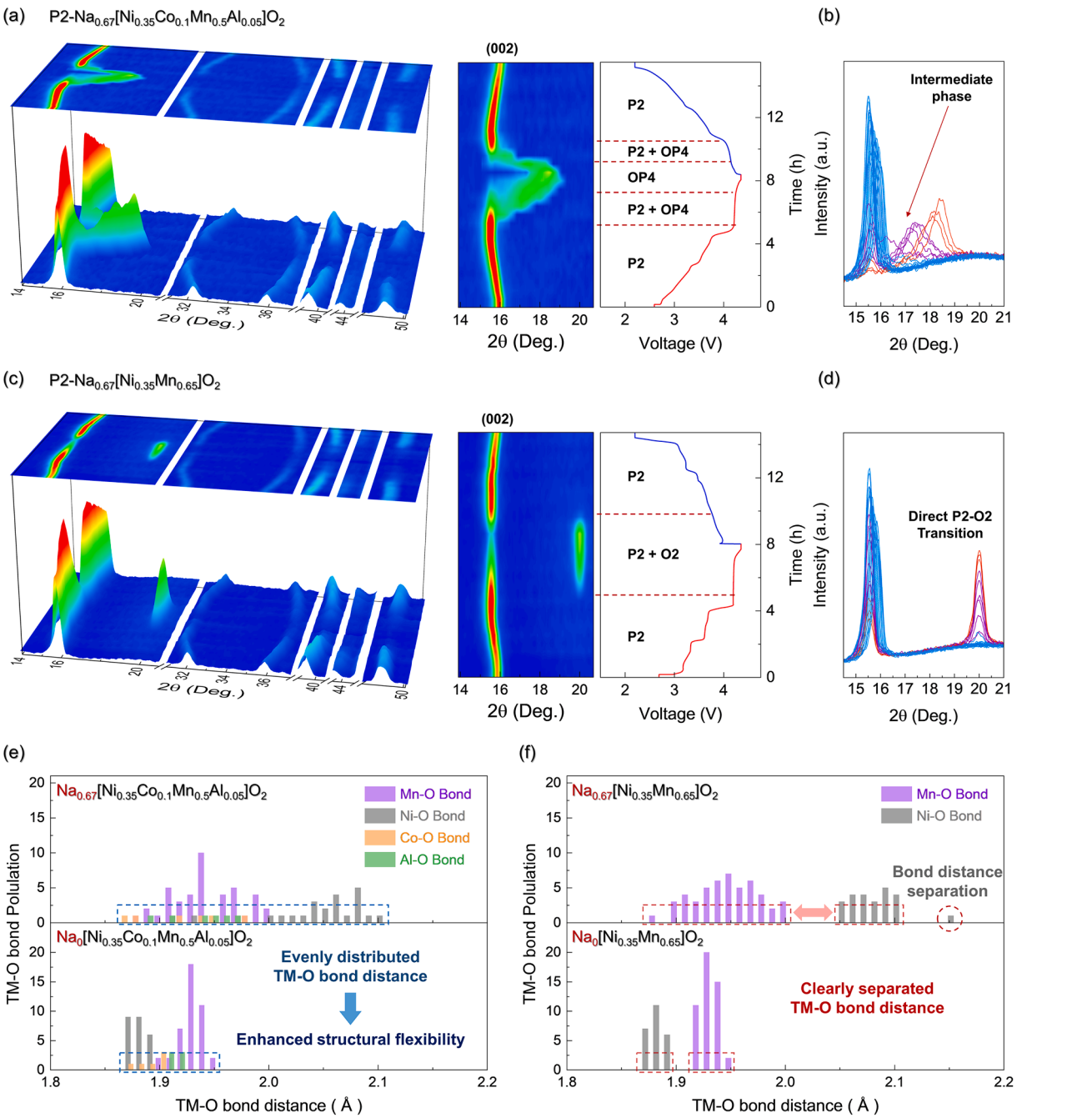

Fig. 3. (a) *Operando* XRD patterns, magnified views, voltage profile and (b) non-stacking views of P2-$Na_{0.67}[Ni_{0.35}Co_{0.1}Mn_{0.5}Al_{0.05}]O_2$ during charge/discharge. (c) *Operando* XRD patterns, magnified views, voltage profile and (d) non-stacking views of P2-$Na_{0.67}[Ni_{0.35}Mn_{0.65}]O_2$ during charge/discharge. TM-O bond population of (e) P2-$Na_{0.67}[Ni_{0.35}Co_{0.1}Mn_{0.5}Al_{0.05}]O_2$ and (f) P2-$Na_{0.67}[Ni_{0.35}Mn_{0.65}]O_2$.

which in turn leads to improved structural stability. Moreover, these results are well-matched with the *operando* XRD data on P2-NCMA, which shows continuous and smooth structural changes during charge/discharge without a clear phase transition between the P2 and OP4 phases, distinct from P2-NM.

3.4. *Improved kinetics of redox reactions in P2-$Na_{0.67}[Ni_{0.35}Co_{0.1}Mn_{0.5}Al_{0.05}]O_2$ through introduction of structural flexibility*

As illustrated in Fig. 4a-b, we conducted a comprehensive investigation into the theoretical motion of Na^+ diffusion and the required activation barrier energies in both P2-NCMA and P2-NM, employing the nudged elastic band (NEB) method based on first-principles calculation. The results unequivocally demonstrated that the required Na^+ diffusion barrier energy in P2-NCMA (~409 meV) is lower than that in P2-NM (~602 meV), underscoring the improved Na^+ diffusion kinetics in P2-NCMA. To verify these results experimentally, moreover, we conducted the Galvanostatic intermittent titration technique (GITT) test which is introduced by Weppent and Huggins [43,44]. When a constant current is applied to an electrode, it leads to the establishment of a Na^+ ion concentration gradient on both the surface and inside the electrode during cycling. Assuming that Na^+ ion transport in the electrode adheres to Fick's 2nd law, the Na^+ diffusivity can be determined by monitoring the potential variation with respect to the state-of-charge (SOC), as depicted in Fig. 4c-d (Eq. (1)).

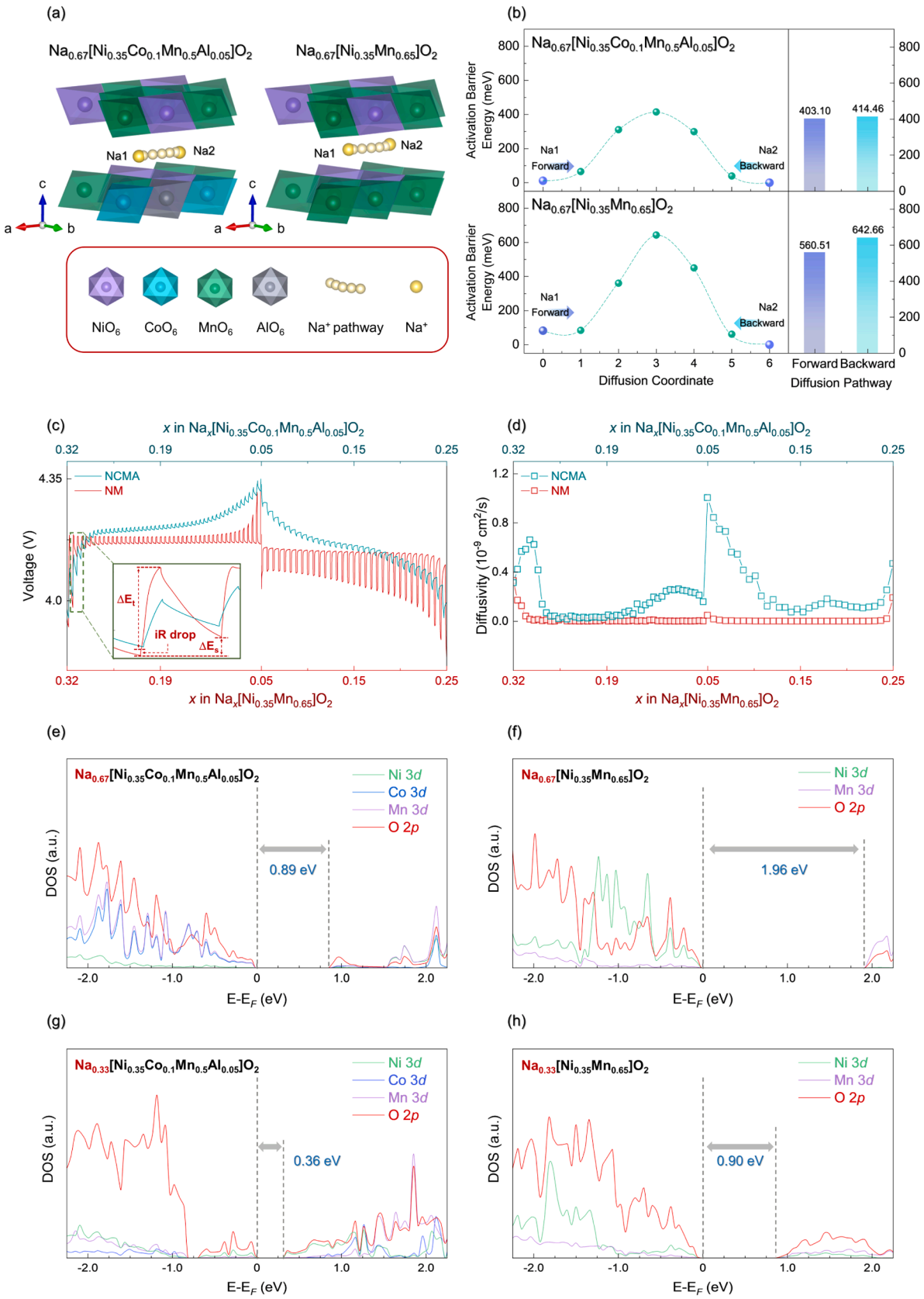

Fig. 4. (a) Predicted Na^+ diffusion pathway in P2-$Na_{0.67}[Ni_{0.35}Co_{0.1}Mn_{0.5}Al_{0.05}]O_2$ and P2-$Na_{0.67}[Ni_{0.35}Mn_{0.65}]O_2$ and (b) predicted activation barrier energy for Na^+ diffusion. (c) GITT test profiles and (d) diffusivity results of P2-$Na_{0.67}[Ni_{0.35}Co_{0.1}Mn_{0.5}Al_{0.05}]O_2$ and P2-$Na_{0.67}[Ni_{0.35}Mn_{0.65}]O_2$ at high voltage region. The density of states for (e) P2-$Na_{0.67}[Ni_{0.35}Co_{0.1}Mn_{0.5}Al_{0.05}]O_2$ and (f) P2-$Na_{0.67}[Ni_{0.35}Mn_{0.65}]O_2$ at pristine state. The density of states for (g) P2-$Na_{0.33}[Ni_{0.35}Co_{0.1}Mn_{0.5}Al_{0.05}]O_2$ and (h) P2-$Na_{0.33}[Ni_{0.35}Mn_{0.65}]O_2$ at just before phase transition state.

$$D = \frac{4}{\pi\tau}\left(\frac{mV}{MS}\right)^2\left(\frac{\Delta E_s}{\Delta E_t}\right)^2, \left(\tau \ll \frac{L^2}{D}\right) \quad (1)$$

In the Eq. (1), D represents the diffusion coefficient of Na^+, τ denotes the duration of application of constant current, m stands for the electrode's mass, V signifies the molar volume of the electrode, M corresponds to the molar mass of electrode, S designates the surface area of contact between the electrode and electrolyte, ΔE_s represents the voltage change during a single step, and ΔE_t reflects the cumulative voltage change under applied constant current conditions.

Through the Eq. (1), we calculated the diffusivity of P2-NCMA and P2-NM. It was revealed that P2-NCMA exhibited a value of ~1.24 × 10^{-9} cm^2 s^{-1} at low voltage region below 4.0 V (*vs.* Na^+/Na) and decreased to ~2.26 × 10^{-10} cm^2 s^{-1} at high voltage region above 4.0 V (*vs.* Na^+/Na). In contrast, P2-NM displayed a value of ~1.11 × 10^{-9} cm^2 s^{-1} at low voltage region and significantly decreased to ~3.19 × 10^{-11} cm^2 s^{-1} at the high voltage region (Fig. S24). This analysis indicates that in the low voltage region below 4.0 V (*vs.* Na^+/Na), there is not a significant difference between P2-NCMA and P2-NM. However, in the high voltage region above 4.0 V (*vs.* Na^+/Na), P2-NCMA exhibits approximately seven times higher diffusivity compared to P2-NM. Moreover, electrochemical impedance spectroscopy (EIS) [45,46], as depicted in Fig. S25, was carried out to access the diffusion kinetics of P2-NCMA and P2-NM. The semi-circle size for P2-NCMA (~73 Ω), associated with the resistance to Na^+ charge transfer, was notably smaller than that observed for P2-NM (~120 Ω). This indicates a significant acceleration of Na^+ diffusion rate in P2-NCMA, providing additional evidence of enhanced electrochemical performance.

In addition, using first-principles calculation, it was demonstrated that P2-NCMA exhibits the enhanced electronic conductivity compared to P2-NM. As shown in Fig. 4e-f, the density of states (DOS) for pristine P2-NCMA and P2-NM indicates that P2-NCMA exhibits a low band gap of 0.89 eV, whereas P2-NM shows a significantly larger band gap of 1.96 eV Furthermore, Fig. 4g-h presents the band gap just before phase transition, revealing that P2-type $Na_{0.33}[Ni_{0.35}Co_{0.1}Mn_{0.5}Al_{0.05}]O_2$ (P2-$Na_{0.33}$NCMA) has a very small band gap of 0.36 eV, while P2-type $Na_{0.33}[Ni_{0.35}Mn_{0.65}]O_2$ (P2-$Na_{0.33}$NM) delivered a band gap of 0.90 eV It was reported that the small band gap typically indicates high electronic conductivity [47,48]. Thus, these DOS results indicate the highly enhanced electronic conductivity of P2-NCMA compared to P2-NM. Through these findings, we confirmed that Co-Al co-substitution in the structure increases the distance between Na layers, effectively enhancing structural flexibility, facilitating greater Na^+ diffusion, and reducing the band gap. This correlation suggests that increased structural flexibility enables the outstanding electrochemical performance of P2-NCMA through the enhanced ionic conductivity and electronic conductivities. Especially, upon comparing with other reported Ni-Mn-based P2-type layered oxide cathodes (Table S6) [16,32,49–53], it was evident that P2-NCMA exhibited remarkably high energy density and outstanding power-capability as the promising cathode for SIBs (Fig. 5).

3.5. Reaction mechanism in P2-$Na_{0.67}[Ni_{0.35}Co_{0.1}Mn_{0.5}Al_{0.05}]O_2$ during charge/discharge

To confirm the detailed redox reactions in P2-NCMA, we performed first-principles calculation and various experiments. Fig. 6a illustrates the variations in DOS for P2-NCMA based on the Na^+ content in the structure. It was verified that Co and Ni ions in P2-NCMA participate in the redox reaction during Na^+ de/intercalation, which is also confirmed through the synchrotron-based *ex-situ* XANES analyses. For the Ni K-edge, it was noticeably shifted toward the high energy level during charging to 4.35 V (*vs.* Na^+/Na), reflecting increase of the oxidation state of Ni ions as the voltage rises (Fig. 6b). During discharge, the Ni K-edge was re-shifted to the pristine state, indicating the reversible redox reaction of Ni ions in P2-NCMA. The reversible redox reaction of Co ions in P2-NCMA during charge/discharge was also clearly observed (Fig. 6c). In the case of Mn ions, its oxidation state was well maintained to +4 during charge/discharge (Fig. 6d). Moreover, when observed through L-edge TEY-PES, it was noted that as Ni ions underwent the oxidation from the 2.5+ to 4+ during charge, there was an increase in the intensity in the L3 region (Fig. S26a) [54]. For Co ions, an increase in voltage led to an intensity rise in both the L3 and L2 regions, indicating the oxidation from Co^{3+} to Co^{4+} during charge (Fig. S26b) [55]. This provides further evidence on reversible occurrence of the oxidation reactions for both Ni and Co ions during the charging process. Additionally, we arranged the capacity contribution of the Ni and Co ions in P2-NCMA (Table S7) in detail. Furthermore, to investigate whether redox activity occurs with oxygen, we performed oxygen K-edge soft-XAS analysis on both P2-NCMA and P2-NM in their pristine and fully charged states (Fig. S27a-b). The pre-edge peak at approximately 529 eV corresponds to the unoccupied TM 3*d*-O 2*p* t_{2g} hybridized orbitals, while the e_g orbitals are found near 531.4 eV [56]. If an oxygen redox reaction had taken place, we would anticipate an increase in

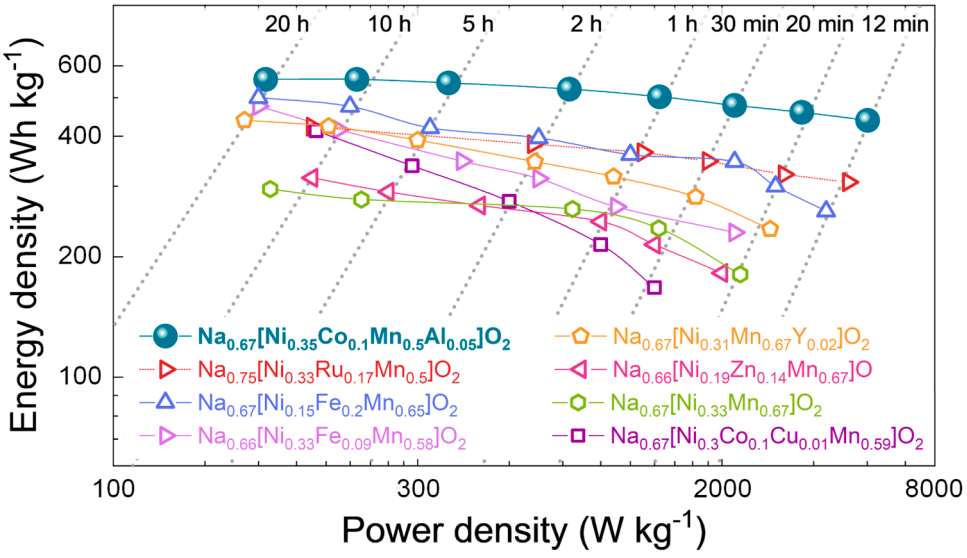

Fig. 5. Comparison of energy and power densities among P2-$Na_{0.67}[Ni_{0.35}Co_{0.1}Mn_{0.5}Al_{0.05}]O_2$ and other reported Ni-Mn-based P2-type layered oxide cathodes for SIBs.

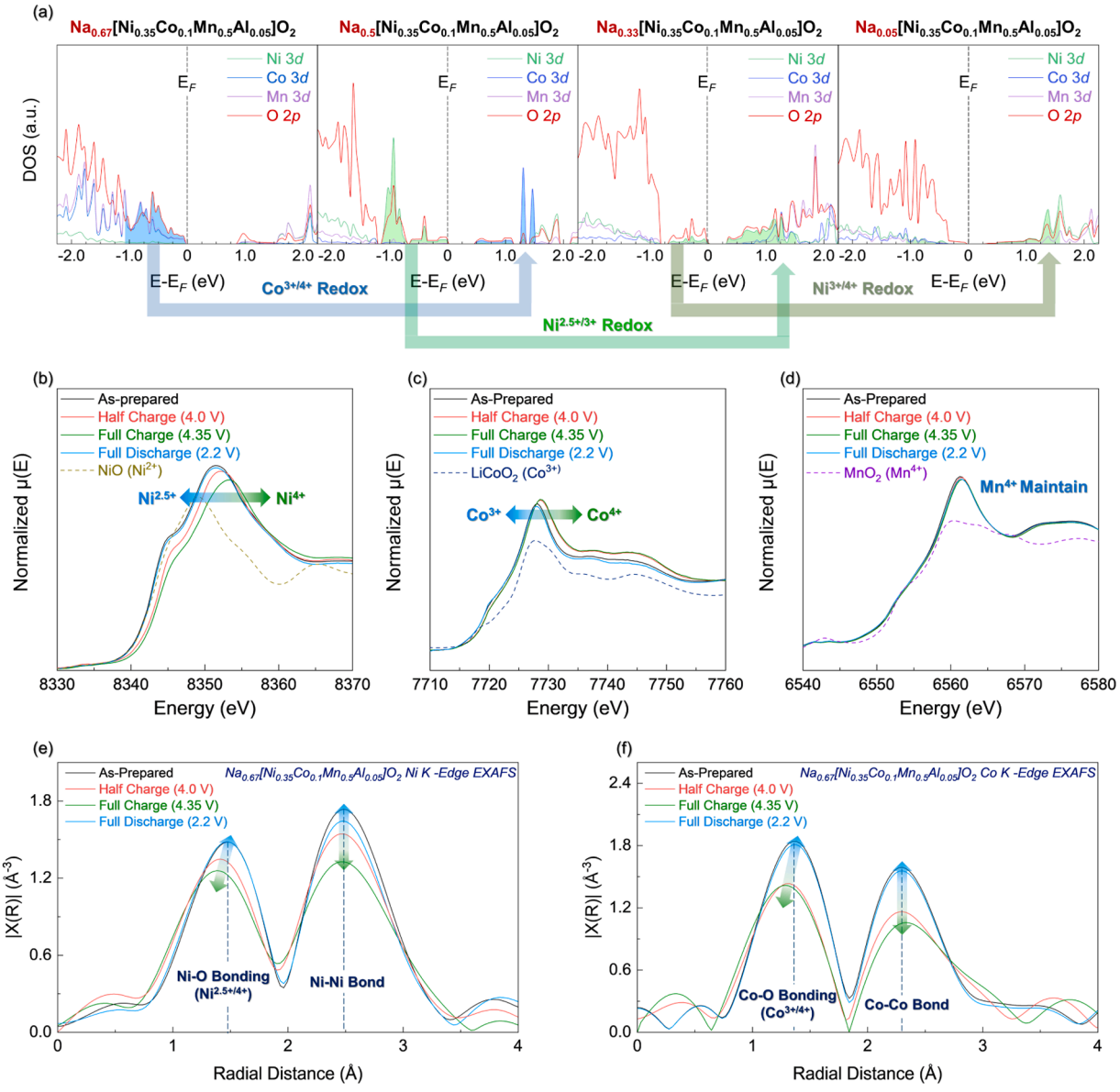

Fig. 6. (a) Projected density of states (pDOS) of Ni-3*d*, Co-3*d*, Mn-3*d* and O-2*p* at $Na_x[Ni_{0.35}Co_{0.1}Mn_{0.5}Al_{0.05}]O_2$ ($0.05 \leq x \leq 0.67$). *Ex-situ* (b) Ni, (c) Co and (d) Mn K-edge XANES spectra of various state of $Na_{0.67}[Ni_{0.35}Co_{0.1}Mn_{0.5}Al_{0.05}]O_2$. (e) Ni K-edge and (f) Co K-edge EXAFS analyses of various charge/discharge state of P2-$Na_{0.67}[Ni_{0.35}Co_{0.1}Mn_{0.5}Al_{0.05}]O_2$.

absorbance at 530.4 eV, associated with O^{n-} species in the oxidized state of oxygen [57]. However, only negligible increase in absorbance at 530.4 eV was observed in the fully charged P2-NCMA and P2-NM samples, which indicates that the oxygen redox activity is not observed in P2-NCMA and P2-NM cathodes. In addition, the slight change of the overall shape of the O K-edge spectra after charge is attributed to local structural changes by oxidation of transition metal ions, such as Ni, Co, *etc* [58]. Especially, the *ex-situ* EXAFS results showed the reversible local structural change in P2-NCMA during charge/discharge through enhanced structural flexibility. As shown in Fig. 6e-f, the Ni-O and Co-O bond distances were observed to decrease during charging due to the oxidation of Ni and Co ions, and they fully recovered to their pristine states after discharging. These behaviors are associated with smooth redox reactions and enhanced electrochemical performances in P2-NCMA.

4. Conclusion

This research showed that introducing structural flexibility can significantly enhance electrochemical performances, such as high power-capability, outstanding fast charging/discharging performances including lowered overpotential and stable cycle-performance, for P2-type Ni-Mn-based Na-layered cathodes. In the case of the P2-NCMA cathode, it delivered high discharge capacity and energy density of ~156.31 mAh g^{-1} and ~551.71 Wh kg^{-1} at 10 mA g^{-1}, respectively, which are larger than those of P2-NM cathode. Particularly, even at 1000 mA g^{-1}, the capacity and energy density of P2-NCMA are still retained to ~132.38 mAh g^{-1} and ~440.90 Wh kg^{-1}, whereas P2-NM cathode just delivered ~94.31 mAh g^{-1} and ~286.31 Wh kg^{-1} at the same conditions. The large difference of energy densities between P2-NCMA and P2-NM at 1000 mA g^{-1} is attributed to smaller voltage gap of P2-NCMA at the high voltage region than those of P2-NM. It was revealed the large difference of energy densities between P2-NCMA and P2-NM at 1000 mA g^{-1} attributed to highly lowered operation voltage of

P2-NM at the high voltage region by large overpotential compared to P2-NCMA, which is well matched with ~7 times higher diffusivity of P2-NCMA in the high voltage range above 4.0 V (*vs.* Na^+/Na) compared to P2-NM. Moreover, comparison of theoretical DOS and Na^+ diffusion kinetics showed that P2-NCMA delivered improved electronic and Na^+ ionic conduction than P2-NM, which also supports the enhanced power-capability and fast charging/discharging performances in P2-NCMA. In terms of the enhanced structural flexibility by Co-Al co-substitution in P2-NCMA, it was clearly demonstrated through combined studies using *operando* XRD analyses and first-principles calculation. While it was revealed that P2-NM undergoes the direct P2-O2 phase transition during charge/discharge, P2-NCMA exhibited the relatively smooth and continuous structural change during charge/discharge, indicating the effect of the enhanced structural flexibility in P2-NCMA. Moreover, by analyzing the TM-O bond distance distribution during Na^+ de/intercalation, the TM-O bond distances in P2-NM are clearly separated, whereas those in P2-NCMA are well distributed without clear separation. This suggests that the P2-NCMA structure experiences relatively less lattice mismatch and strain during charge/discharge compared to P2-NM, which can explain the differences observed in the *operando* XRD results between P2-NCMA and P2-NM. In the case of the cycle-performance, P2-NCMA also exhibited better performance than P2-NM, resulting from the enhanced structural flexibility. We believe that our research provides valuable insights into discovering efficient and straightforward methods for enhancing both high power-capability and stable cycle-performance in layered-type cathode materials for Na-ion batteries.

CRediT authorship contribution statement

Bonyoung Ku: Writing – original draft, Visualization, Validation, Investigation, Data curation, Conceptualization. **Jinho Ahn:** Writing – original draft, Visualization, Formal analysis, Data curation, Conceptualization. **Hoseok Lee:** Validation, Methodology. **Hobin Ahn:** Methodology, Investigation. **Jihoe Lee:** Visualization, Validation. **Hyunji Kweon:** Visualization, Formal analysis. **Myungeun Choi:** Visualization, Formal analysis. **Hun-Gi Jung:** Validation, Conceptualization. **Kyu-wook Ihm:** Data curation, Visualization. **Eunji Sim:** Formal analysis, Visualization. **Jung-Keun Yoo:** Supervision, Validation, Visualization, Writing – review & editing. **Jongsoon Kim:** Writing – review & editing, Visualization, Supervision, Investigation, Funding acquisition, Data curation, Conceptualization.

Declaration of competing interest

The authors declare that they have no known competing financial interests or personal relationships that could have appeared to influence the work reported in this paper.

Acknowledgement

This work was supported by the Technology Innovation Program (RS-2024–00403571, Development of high-capacity layered oxide cathode material for sodium ion battery) funded by the Ministry of Trade, Industry & Energy (MOTIE, Korea). In addition, the calculation resources were supported by the Supercomputing Center in Korea Institute of Science and Technology Information (KISTI) (KSC-2023-CRE-0440).

Supplementary materials

Supplementary material associated with this article can be found, in the online version, at doi:10.1016/j.ensm.2024.103930.

Data availability

Data will be made available on request.

References

[1] R. Qian, Y. Liu, T. Cheng, P. Li, R. Chen, Y. Lyu, B. Guo, Enhanced surface chemical and structural stability of Ni-rich cathode materials by synchronous lithium-ion conductor coating for lithium-ion batteries, ACS Appl. Mater. Interfaces. 12 (2020) 13813–13823, https://doi.org/10.1021/acsami.9b21264.
[2] S. Bashir, P. Hanumandla, H.Y. Huang, J.L. Liu, Nanostructured materials for advanced energy conversion and storage devices: Safety implications at end-of-life disposal, Nanostruct. Mater. Next-Generat. Energy Storage Convers. Fuel Cells. 4 (2018) 517–542, https://doi.org/10.1007/978-3-662-56364-9_18.
[3] G.L. Soloveichik, Battery technologies for large-scale stationary energy storage, Annu. Rev. Chem. Biomol. Eng. 2 (2011) 503–527, https://doi.org/10.1146/annurev-chembioeng-061010-114116.
[4] J.B. Goodenough, How we made the Li-ion rechargeable battery: Progress in portable and ubiquitous electronics would not be possible without rechargeable batteries. John B. Goodenough recounts the history of the lithium-ion rechargeable battery, Nat. Electron. 1 (2018) 204, https://doi.org/10.1038/s41928-018-0048-6.
[5] J. Ahn, J. Kang, M.-K. Cho, H. Park, W. Ko, Y. Lee, H. Kim, Y.H. Jung, T.-Y. Jeon, H. Kim, W.-H. Ryu, J. Hong, J. Kim, Selective anionic redox and suppressed structural disordering enabling high-energy and long-life li-rich layered-oxide cathode, Adv. Energy Mater. 11 (2021) 2102311, https://doi.org/10.1002/aenm.202102311.
[6] F. Duffner, M. Wentker, M. Greenwood, J. Leker, Battery cost modeling: a review and directions for future research, Renew. Sustain. Energy Rev. 127 (2020) 109872, https://doi.org/10.1016/j.rser.2020.109872.
[7] S. Randau, D.A. Weber, O. Kötz, R. Koerver, P. Braun, A. Weber, E. Ivers-Tiffée, T. Adermann, J. Kulisch, W.G. Zeier, F.H. Richter, J. Janek, Benchmarking the performance of all-solid-state lithium batteries, Nat. Energy. 5 (2020) 259–270, https://doi.org/10.1038/s41560-020-0565-1.
[8] Y. Lee, H. Park, M. Kyung Cho, J. Ahn, W. Ko, J. Kang, Y.J. Choi, H. Kim, I. Park, W. H. Ryu, J. Hong, J. Kim, Li-Rich Mn–Mg layered oxide as a novel Ni-/Co-Free cathode, Adv. Funct. Mater. 32 (2022) 1–13, https://doi.org/10.1002/adfm.202204354.
[9] F. Duffner, N. Kronemeyer, J. Tübke, J. Leker, M. Winter, R. Schmuch, Post-lithium-ion battery cell production and its compatibility with lithium-ion cell production infrastructure, Nat. Energy. 6 (2021) 123–134, https://doi.org/10.1038/s41560-020-00748-8.
[10] J. Ahn, H. Park, W. Ko, Y. Lee, J. Kang, S. Lee, S. Lee, E. Sim, K. Ihm, J. Hong, J. K. Yoo, K. Ku, J. Kim, Occurrence of anionic redox with absence of full oxidation to Ru5+ in high-energy P2-type layered oxide cathode, J. Energy Chem. 84 (2023) 153–161, https://doi.org/10.1016/j.jechem.2023.05.016.
[11] P.K. Nayak, L. Yang, W. Brehm, P. Adelhelm, From lithium-ion to sodium-ion batteries: advantages, challenges, and surprises, Angew. Chemie - Int. Ed. 57 (2018) 102–120, https://doi.org/10.1002/anie.201703772.
[12] V. Palomares, P. Serras, I. Villaluenga, K.B. Hueso, J. Carretero-González, T. Rojo, Na-ion batteries, recent advances and present challenges to become low cost energy storage systems, Energy Environ. Sci. 5 (2012) 5884–5901, https://doi.org/10.1039/c2ee02781j.
[13] W. Ko, M.-K. Cho, J. Kang, H. Park, J. Ahn, Y. Lee, S. Lee, S. Lee, K. Heo, J. Hong, J.-K. Yoo, J. Kim, Exceptionally increased reversible capacity of O3-type NaCrO2 cathode by preventing irreversible phase transition, Energy Storage Mater. 46 (2022) 289–299, https://doi.org/10.1016/j.ensm.2022.01.023.
[14] C. Masquelier, L. Croguennec, Polyanionic (phosphates, silicates, sulfates) frameworks as electrode materials for rechargeable Li (or Na) batteries, Chem. Rev. 113 (2013) 6552–6591, https://doi.org/10.1021/cr3001862.
[15] B. Xie, B. Sun, T. Gao, Y. Ma, G. Yin, P. Zuo, Recent progress of Prussian blue analogues as cathode materials for nonaqueous sodium-ion batteries, Coord. Chem. Rev. 460 (2022) 214478, https://doi.org/10.1016/j.ccr.2022.214478.
[16] S. Kim, K. Min, K. Park, Y-doped P2-type Na0.67Ni0.33Mn0.67O2: A sodium-ion battery cathode with fast charging and enhanced cyclic performance, J. Alloys Compd. 874 (2021) 160027, https://doi.org/10.1016/j.jallcom.2021.160027.
[17] A. Gutierrez, W.M. Dose, O. Borkiewicz, F. Guo, M. Avdeev, S. Kim, T.T. Fister, Y. Ren, J. Bareño, C.S. Johnson, On disrupting the Na+-Ion/vacancy ordering in P2-type sodium-manganese-nickel oxide cathodes for Na+-Ion batteries, J. Phys. Chem. C. 122 (2018) 23251–23260, https://doi.org/10.1021/acs.jpcc.8b05537.
[18] Y. Shi, P. Jiang, S. Wang, W. Chen, B. Wei, X. Lu, G. Qian, W.H. Kan, H. Chen, W. Yin, Y. Sun, X. Lu, Slight compositional variation-induced structural disorder-to-order transition enables fast Na+ storage in layered transition metal oxides, Nat. Commun. 13 (2022), https://doi.org/10.1038/s41467-022-35597-4.
[19] P.F. Wang, H.R. Yao, X.Y. Liu, Y.X. Yin, J.N. Zhang, Y. Wen, X. Yu, L. Gu, Y.G. Guo, Na+/vacancy disordering promises high-rate Na-ion batteries, Sci. Adv. 4 (2018) 1–9, https://doi.org/10.1126/sciadv.aar6018.
[20] B. Ku, H. Ahn, S. Lee, J. Ahn, M. Choi, J. Kang, H. Park, J. Kim, A. Kim, H. Jung, K. Yoo, J. Kim, Stable high-voltage operation of oxygen redox in P2-type Na-layered oxide cathode at fast discharging via enhanced kinetics, Energy Storage Mater. 62 (2023) 102952, https://doi.org/10.1016/j.ensm.2023.102952.
[21] H.H. Ryu, K.J. Park, C.S. Yoon, Y.K. Sun, Capacity fading of ni-rich li[NixCoyMn1-x-y]O2 ($0.6 \leq x \leq 0.95$) cathodes for high-energy-density lithium-ion batteries: bulk or surface degradation? Chem. Mater. 30 (2018) 1155–1163, https://doi.org/10.1021/acs.chemmater.7b05269.

[22] Q. Mao, Y. Yu, J. Wang, L. Zheng, Z. Wang, Y. Qiu, Y. Hao, X. Liu, Mitigating the P2-O2 transition and Na+/vacancy ordering in Na2/3Ni1/3Mn2/3O2by anion/cation dual-doping for fast and stable Na+insertion/extraction, J. Mater. Chem. A. 9 (2021) 10803–10811, https://doi.org/10.1039/d1ta01433a.
[23] C. Zhao, C. Li, Q. Yang, Q. Qiu, W. Tong, S. Zheng, J. Ma, M. Shen, B. Hu, Anionic redox reaction in Na-deficient layered oxide cathodes: Role of Sn/Zr substituents and in-depth local structural transformation revealed by solid-state NMR, Energy Storage Mater. 39 (2021) 60–69, https://doi.org/10.1016/j.ensm.2021.04.007.
[24] J. Huang, L. Xu, D. Ye, W. Wu, S. Qiu, Z. Tang, X. Wu, Suppressing the P2–O2 phase transition of P2-type Ni/Mn-based layered oxide by synergistic effect of Zn/Ti co-doping for advanced sodium-ion batteries, J. Alloys Compd. 976 (2024) 173397, https://doi.org/10.1016/j.jallcom.2023.173397.
[25] J.B. Goodenough, K.-S. Park, The Li-Ion rechargeable battery: a perspective, J. Am. Chem. Soc. 7 (2013) 26, https://doi.org/10.1021/ja3091438.
[26] C. cheng Fu, J. Wang, Y. Li, G. Liu, T. Deng, Explore the effect of Co Doping on P2-Na0.67MnO2 prepared by hydrothermal method as cathode materials for sodium ion batteries, J. Alloys Compd. 918 (2022) 165569, https://doi.org/10.1016/j.jallcom.2022.165569.
[27] N. Bucher, S. Hartung, J.B. Franklin, A.M. Wise, L.Y. Lim, H.Y. Chen, J.N. Weker, M.F. Toney, M. Srinivasan, P2-NaxCoyMn1-yO2 (y = 0, 0.1) as cathode materials in sodium-ion batteries - effects of doping and morphology to enhance cycling stability, Chem. Mater. 28 (2016) 2041–2051, https://doi.org/10.1021/acs.chemmater.5b04557.
[28] P. Hou, F. Li, Y. Wang, J. Yin, X. Xu, Mitigating the P2-O2 phase transition of high-voltage P2-Na 2/3 [Ni 1/3 Mn 2/3]O 2 cathodes by cobalt gradient substitution for high-rate sodium-ion batteries, J. Mater. Chem. A. 7 (2019) 4705–4713, https://doi.org/10.1039/c8ta10980j.
[29] X. Cai, N. Wang, L. Liang, X.L. Li, R. Zhang, L. Ma, E. Hu, S. Shen, Z. Shadike, J. Zhang, Fast oxygen redox kinetics induced by CoO6 octahedron With π-interaction in P2-type sodium oxides, Adv. Funct. Mater. 2409732 (2024) 1–8, https://doi.org/10.1002/adfm.202409732.
[30] W. Xu, Y. Zheng, Y. Cheng, R. Qi, H. Peng, H. Lin, R. Huang, Understanding the effect of Al doping on the electrochemical performance improvement of the LiMn2O4cathode material, ACS Appl. Mater. Interfaces. 13 (2021) 45446–45454, https://doi.org/10.1021/acsami.1c11315.
[31] K. Zhou, Q. Xie, B. Li, A. Manthiram, An in-depth understanding of the effect of aluminum doping in high-nickel cathodes for lithium-ion batteries, Energy Storage Mater. 34 (2021) 229–240, https://doi.org/10.1016/j.ensm.2020.09.015.
[32] W.L. Pang, X.H. Zhang, J.Z. Guo, J.Y. Li, X. Yan, B.H. Hou, H.Y. Guan, X.L. Wu, P2-type Na2/3Mn1-xAlxO2 cathode material for sodium-ion batteries: Al-doped enhanced electrochemical properties and studies on the electrode kinetics, J. Power Sources. 356 (2017) 80–88, https://doi.org/10.1016/j.jpowsour.2017.04.076.
[33] G. Kresse, J. Furthmüller, Efficiency of ab-initio total energy calculations for metals and semiconductors using a plane-wave basis set, Comput. Mater. Sci. 6 (1996) 15–50, https://doi.org/10.1016/0927-0256(96)00008-0.
[34] P.E. Blöchl, Projector augmented-wave method, Phys. Rev. B. 50 (1994) 17953–17979, https://doi.org/10.1103/PhysRevB.50.17953.
[35] J.P. Perdew, K. Burke, M. Ernzerhof, Generalized gradient approximation made simple, Phys. Rev. Lett. 77 (1996) 3865–3868, https://doi.org/10.1103/PhysRevLett.77.3865.
[36] A. Jain, G. Hautier, S.P. Ong, C.J. Moore, C.C. Fischer, K.A. Persson, G. Ceder, Formation enthalpies by mixing GGA and GGA + U calculations, Phys. Rev. B - Condens. Matter Mater. Phys. 84 (2011) 1–10, https://doi.org/10.1103/PhysRevB.84.045115.
[37] J. Heyd, G.E. Scuseria, M. Ernzerhof, Hybrid functionals based on a screened coulomb potential, J. Chem. Phys. 118 (2003) 8207–8215, https://doi.org/10.1063/1.1564060.
[38] A. Van der Ven, J.C. Thomas, Q. Xu, J. Bhattacharya, Linking the electronic structure of solids to their thermodynamic and kinetic properties, Math. Comput. Simul. 80 (2010) 1393–1410, https://doi.org/10.1016/j.matcom.2009.08.008.
[39] T. Risthaus, D. Zhou, X. Cao, X. He, B. Qiu, J. Wang, L. Zhang, Z. Liu, E. Paillard, G. Schumacher, M. Winter, J. Li, A high-capacity P2 Na2/3Ni1/3Mn2/3O2 cathode material for sodium ion batteries with oxygen activity, J. Power Sources. 395 (2018) 16–24, https://doi.org/10.1016/j.jpowsour.2018.05.026.
[40] Y. Chen, G. Su, X. Cheng, T. Du, Y. Han, W. Qiang, B. Huang, Electrochemical performances of P2-Na2/3Ni1/3Mn2/3O2 doped with Li and Mg for high cycle stability, J. Alloys Compd. 858 (2021) 157717, https://doi.org/10.1016/j.jallcom.2020.157717.
[41] C. Cai, X. Li, P. Hu, T. Zhu, J. Li, H. Fan, R. Yu, T. Zhang, S. Lee, L. Zhou, L. Mai, Comprehensively strengthened metal-oxygen bonds for reversible anionic redox reaction, Adv. Funct. Mater. 33 (2023) 1–8, https://doi.org/10.1002/adfm.202215155.
[42] H. Gao, J. Li, F. Zhang, C. Li, J. Xiao, X. Nie, G. Zhang, Y. Xiao, D. Zhang, X. Guo, Y. Wang, Y.M. Kang, G. Wang, H. Liu, Revealing the potential and challenges of high-entropy layered cathodes for sodium-based energy storage, Adv. Energy Mater. 14 (2024) 1–18, https://doi.org/10.1002/aenm.202304529.
[43] W. Weppner, R.A. Huggins, Determination of the kinetic parameters of mixed-conducting electrodes and application to the system Li3Sb, J. Electrochem. Soc. 124 (1977) 1569–1578, https://doi.org/10.1149/1.2133112.
[44] A.P. Nowak, B. Wicikowska, K. Trzciński, A. Lisowska-Oleksiak, Determination of chemical diffusion coefficient of lithium ions in ceramics derived from pyrolysed poly(1,2-dimethylsilazane) and starch, Procedia Eng. 98 (2014) 8–13, https://doi.org/10.1016/j.proeng.2014.12.480.
[45] P. Gupta, S. Pushpakanth, M.A. Haider, S. Basu, Understanding the design of cathode materials for Na-Ion batteries, ACS. Omega 7 (2022) 5605–5614, https://doi.org/10.1021/acsomega.1c05794.
[46] W. Kong, H. Wang, L. Sun, C. Su, X. Liu, Understanding the synergic roles of MgO coating on the cycling and rate performance of Na0.67Mn0.5Fe0.5O2 cathode, Appl. Surf. Sci. 497 (2019) 143814, https://doi.org/10.1016/j.apsusc.2019.143814.
[47] A.J. Garza, G.E. Scuseria, Predicting band gaps with hybrid density functionals, J. Phys. Chem. Lett. 7 (2016) 4165–4170, https://doi.org/10.1021/acs.jpclett.6b01807.
[48] A. Shaheen, J. Alam, M.S. Anwar, Band structure and electrical conductivity in semiconductors, Mater. Eng. (2010) 1–26.
[49] Q. Wang, K. Jiang, Y. Feng, S. Chu, X. Zhang, P. Wang, S. Guo, H. Zhou, P2-Type Layered Na0.75Ni1/3Ru1/6Mn1/2O2cathode material with excellent rate performance for sodium-ion batteries, ACS Appl. Mater. Interfaces. 12 (2020) 39056–39062, https://doi.org/10.1021/acsami.0c09082.
[50] D. Yuan, X. Hu, J. Qian, F. Pei, F. Wu, R. Mao, X. Ai, H. Yang, Y. Cao, P2-type Na0.67Mn0.65Fe0.2Ni 0.15O2 cathode material with high-capacity for sodium-ion battery, Electrochim. Acta. 116 (2014) 300–305, https://doi.org/10.1016/j.electacta.2013.10.211.
[51] Q. Yang, P.F. Wang, J.Z. Guo, Z.M. Chen, W.L. Pang, K.C. Huang, Y.G. Guo, X. L. Wu, J.P. Zhang, Advanced P2-Na2/3Ni1/3Mn7/12Fe1/12O2 cathode material with suppressed P2-O2 phase transition toward high-performance sodium-ion battery, ACS Appl. Mater. Interfaces. 10 (2018) 34272–34282, https://doi.org/10.1021/acsami.8b12204.
[52] X. Wu, J. Guo, D. Wang, G. Zhong, M.J. McDonald, Y. Yang, P2-type Na0.66Ni0.33-xZnxMn0.67O2 as new high-voltage cathode materials for sodium-ion batteries, J. Power Sources. 281 (2015) 18–26, https://doi.org/10.1016/j.jpowsour.2014.12.083.
[53] B. Tiwari, I. Bhattacharya, Layered P2- type novel Na0.7Ni0.3Mn0.59Co0.1Cu0.01O2 cathode material for high-capacity & stable rechargeable sodium ion battery, Electrochim. Acta. 270 (2018) 363–368, https://doi.org/10.1016/j.electacta.2018.03.058.
[54] C. Hakim, N. Sabi, L.A. Ma, M. Dahbi, D. Brandell, K. Edström, L.C. Duda, I. Saadoune, R. Younesi, Understanding the redox process upon electrochemical cycling of the P2-Na0.78Co1/2Mn1/3Ni1/6O2 electrode material for sodium-ion batteries, Commun. Chem. 3 (2020), https://doi.org/10.1038/s42004-020-0257-6.
[55] F. Zhang, S. Lou, S. Li, Z. Yu, Q. Liu, A. Dai, C. Cao, M.F. Toney, M. Ge, X. Xiao, W. K. Lee, Y. Yao, J. Deng, T. Liu, Y. Tang, G. Yin, J. Lu, D. Su, J. Wang, Surface regulation enables high stability of single-crystal lithium-ion cathodes at high voltage, Nat. Commun. (2020) 11, https://doi.org/10.1038/s41467-020-16824-2.
[56] G. Assat, D. Foix, C. Delacourt, A. Iadecola, R. Dedryvère, J.M. Tarascon, Fundamental interplay between anionic/cationic redox governing the kinetics and thermodynamics of lithium-rich cathodes, Nat. Commun. 8 (2017), https://doi.org/10.1038/s41467-017-02291-9.
[57] W.E. Gent, I.I. Abate, W. Yang, L.F. Nazar, W.C. Chueh, Design rules for high-valent redox in intercalation electrodes, Joule 4 (2020) 1369–1397, https://doi.org/10.1016/j.joule.2020.05.004.
[58] J.P. Singh, J.Y. Park, K.H. Chae, D. Ahn, S. Lee, Soft x-ray absorption spectroscopic investigation of li(Ni0.8 co0.1 mn0.1)o2 cathode materials, Nanomaterials 10 (2020) 1–11, https://doi.org/10.3390/nano10040759.